Peer-reviewed version available at *Appl. Sci.* **2019**, *9*, 2920; doi:10.3390/app9142920

Article

Visualization of the Strain-rate State of a Data Cloud: Analysis of the Temporal Change of an Urban Multivariate Description

Lorena Salazar-Llano [1,3], Camilo Bayona-Roa [2,3]*

1 Sustainability Measurement and Modeling Lab., Universitat Politecnica de Catalunya – Barcelona Tech, Barcelona (Spain); E-Mail: lorena.salazar.l@upc.edu (L. S.-L.)
2 Universidad Nacional de Colombia, Bogotá (Colombia); E-Mail: cabayonar@unal.edu.co (C. B.-R.)
3 Centro de Ingeniería Avanzada, Investigación y Desarrollo – CIAID, Bogotá (Colombia)
* Correspondence: cabayonar@unal.edu.co

Abstract: One challenging problem is the representation of three-dimensional datasets that vary with time. These datasets can be though as a cloud of points that gradually deforms. But point-wise variations lack of information about the overall deformation pattern, and more importantly, about the extreme deformation locations inside the cloud. The present article applies a technique in computational mechanics to derive the strain-rate state of a time-dependent and three-dimensional data distribution, by which one can characterize its main trends of shift. Indeed, the tensorial analysis methodology is able to determine the global deformation rates in the entire dataset. With the use of this technique, one can characterize the significant fluctuations in a reduced multivariate description of an urban system and identify the possible causes of those changes: calculating the strain-rate state of a PCA-based multivariate description of an urban system, we are able to describe the clustering and divergence patterns between the districts of the city and to characterize the temporal rate in which those variations happen.

Keywords: dimensionality reduction; pattern identification; three-dimensional data-cloud; strain-rate; Finite Element Method (FEM); trajectory visualization

1. Introduction

One challenging problem in the data analysis is the representation of three-dimensional discrete data [1]. This analysis becomes harder when a time-dependent change of the data takes place, introducing a new temporal dimension. In the present article, we explore formal approaches to quantify the temporal change of discrete three-dimensional data. Specifically, we build a methodology to assess the transformation of a data cloud that is derived from a *Principal Component Analysis*(PCA): a 13-years span multivariate description in [2] that provides a reduced description of an urban system given only by the first three principal components. Since the points represent an abstraction of an urban system, one main goal is to understand the temporal variation of the multivariate description of the districts in order to analyze the behavior of the overall city in the time-span. Our main hypothesis is that these three-dimensional datasets can be though as a cloud of points that gradually deforms.

Still, the challenging issue is that deformation between consecutive times cannot be visualized straightforwardly. There are some methods to overcome this difficulty. One is the vector plot of three-dimensional displacements or velocities, that is typically used to visualize results in Computational Mechanics applications [3–5]. In example, these are used in the Kinematic Visualization of Motion in [6–10], but they are restricted to display relative motion among the data, and are not able to identify the most dynamic regions of the dataset. Another is the Parallel Coordinate Technique that successfully exhibits the temporal change of highly-dimensional statistical and information datasets [11]. Yet, multi-dimensional data is typically segmented in two-dimensional subsets, like the Computer Tomographic scans of medical imaging [1,12,13]. Furthermore, the previously mentioned methods are not suitable when one aim to understand the patterns of diversification or conformation, which are closely related to the temporal change of the differences between join data values: the maximum and minimum magnitudes of variation and the evaluation of their direction can be significantly helpful when one aims to identify differentiation patterns in the data [14]. Or the opposite, when one aims to locate uniformity for a dataset which was previously differentiated.

The field of continuum mechanics provides a measure of the temporal variation of the distance in between points: *the Strain-Rate tensor* (see, for instance, [15]). The continuum mechanics theory -which arises from the classical Newtonian mechanics- analyzes the causes and effects of motion for a deformable media composed by an infinite group of particles. When a continuous media is being deformed in various directions at different rates, the strain-rate of a certain position in the medium cannot be expressed by a scalar value solely. It cannot even be expressed by using a single vector. Instead, the rate of deformation must be expressed by the rank-two strain-rate tensor with its components determined by the positional derivatives along each spatial dimension. Hence, the mathematical framework of tensors can determine exactly the deformation that is accumulated in a certain position inside the medium -that is typically subjected to the imposition of displacements or loads-. This tensor is commonly used to detail the amount of elastic energy in the physical descriptions of multiple materials, like solids or fluids. See [16] for a complete mathematical exposition. Most of those models are formulated as the product of a constitutive tensor and the strain-rate tensor, giving the stress condition of the material that is balanced in the kinetic equations. In the present study, the calculation of the strain-rate tensor is not related to the kinetics of any material, and thus, it can only be a mathematical tool that supports the examination of the deformation rates given by the discrete statistical data.

But the strain-rate tensor arises from the continuum assumption, and discrete displacements of points rather than continuous distributions take place in the deformation of the data cloud. Typically, the issue of applying derivatives to discrete displacements of points is solved by using several approaches. Some statistical techniques use co-variance functions to represent directly the strain-rate field (see e.g. [17]). But the common approach is to compute a continuous version of the displacement -or velocity- field, so that, derivatives can be applied to the continuous displacements. Some methods, in this line, have interpolated the discrete displacements by minimizing the residual -or distance- between the continuous interpolation and the discrete version [18]. Other interpolation techniques weight the distance between an interpolated piece-wise continuous field and the discrete displacement field, as in [19]. This method results in a minimization technique where a continuous strain-rate field can be derived. In example, the piece-wise continuous field can be defined as to be splines, or as the widely used linear polynomials in variational formulations [20]. These techniques have been applied in earth science and medical imaging works [21–23], but also in the strain-rate calculation of geodetic observations in [24,25].

Another fundamental issue is the representation of the strain-rate state. One of the possible techniques that can help to visualize the deformation rate of the dataset is to plot the main components of the tensor using *Strain-rate diagrams*, where concentrations of strain-rate patterns can be displayed as vector fields (see for example the ones in geodetical observations of the earth's mantle [26–28]). The main drawback of strain-rate diagrams is that the strain-rate components are visualized as the projection of three-dimensional vector fields into the two-dimensional framework, and therefore, the third-dimension component is necessarily neglected. Another method, more suitable to two-dimensional plots, is the contour graph of principal stresses, where the stress patterns in structural elements [29,30] and tectonics [31] are visualized with continuous lines depending on the stress magnitude. That method overcome the three-dimensional issue, but it does not give insights about the orientation of the principal stresses. Hence, a dual form of the contour plots is to calculate the

Preprints (www.preprints.org) | NOT PEER-REVIEWED | Posted: 13 June 2019 doi:10.20944/preprints201906.0114.v1

Peer-reviewed version available at *Appl. Sci.* **2019**, *9*, 2920; doi:10.3390/app9142920

trajectories of the stress principal components in separated plots, where the stress magnitude can be colored in each trajectory line such that stress patterns are exhibited in a two-dimensional framework. This last technique has been our preferred approach in order to visualize the principal strain-rate patterns of the three-dimensional data cloud.

Since a robust methodology that describes the temporal change of the urban system -represented by a multivariate dataset- has not been carried out before, we choose to perform a quantitative analysis by including the strain-rate tensor as the fundamental metric. In this work, we calculate the strain-rate state of the discrete dataset without *a priori* assuming the mechanisms by which the system experiences transformation. In order to apply the continuum mechanics principles into the discrete dataset, we use interpolation methods, such as the ones applied in discrete variational formulations (i.e. *Finite Element Methods* (FEM), Particle Methods, Collocation Methods, Mesh-less methods, etc.). Specifically, we derive the three-dimensional strain-rate tensor from a FEM interpolation of the discrete velocity field, as demonstrated in previous works such as [32–34]. We include a methodology for visualizing the main patterns of change in any time-dependent data cloud that can be used in a computational (two-dimensional) framework. It is based on the family of curves that are instantaneously tangent to the *extension* and *contraction* components of the strain-rate tensor: the so-called *trajectory* curves of the continuum mechanics field [15]. These help to overcome the three-dimensional representation problem, since separated in several plots -one for each principal component-, demonstrate the magnitude and orientations of the strain-rate patterns in a two-dimensional plot.

The remaining parts of this document are organized as follows. In Section 2 the methodology to compute the discrete version of the strain-rate tensor is presented. Since the main problem involves the calculation of the derivatives of discontinuous -discrete- velocities, we extensively review the numerical techniques that are adopted to overcome this difficulty and the ones which are used for visualizing the strain-rate patterns. Next, in Section 3, we present the application of the methodology to the case study -the urban system of Barcelona- by deriving its strain-rate state and visualizing its main strain-rate patterns, meaning the city's environmental, social and economic change. Finally, in Section 4 some conclusions of the proposed methodology close this article.

2. Methods

We begin this section with a review of the strain-rate tensor calculation provided a discrete three-dimensional data cloud. For doing so, the formal problem of the time-dependent dataset is introduced first. Then, we explain the numerical techniques that transform the discrete dataset into a mathematical framework by which the strain-rate tensor can be computed. Most of the ideas rely on the geometrical analysis of the discrete dataset by computing the spatial discretization of the dataset into geometric elements through a *Delaunay Triangulation*. After doing that, the computation of the strain-rate is performed with a FEM interpolation of the velocity field. Finally, we address the *eigen-problem* for the strain-rate tensor, such that the solution of the eigenvalues, and the corresponding eigenvectors, gives the extrema strain-rates at each finite element. The flow chart diagram of this methodology is represented in Fig. 1, including the main outputs that result at each step. The extended explanation is developed along this section.

2.1. Time-dependent three-dimensional dataset

Since the main objective of this work is to reveal the temporal transformation of a three-dimensional and time-dependent dataset, let us first introduce some notation in order to clarify the mathematical ideas to be used. Let us define the discrete time-dependent data to be the set of points $\mathcal{P} = \{p_i\}$, with $i = 1, 2, \ldots, m$, being m the total data. The values in each one of the three dimensions can be seen as scalar coefficients for a set of basis vectors. These tuple of components compose the vector that we call the *position* or *coordinate* $\boldsymbol{x}_i = [x_{i,1} \quad x_{i,2} \quad x_{i,3}]^\top$, with the superscript $\top$ denoting the transpose operation, the first subscript referring to the point i and the second to the dimension. Hence, we call $\mathcal{P}$ the set of *points* and $\mathcal{X}_n(t) = \{\boldsymbol{x}_1(t), \boldsymbol{x}_2(t), \ldots, \boldsymbol{x}_i(t), \ldots, \boldsymbol{x}_n(t)\} \in \mathbb{R}^3$ the *positions* of the

Preprints (www.preprints.org) | NOT PEER-REVIEWED | Posted: 13 June 2019 doi:10.20944/preprints201906.0114.v1
Peer-reviewed version available at Appl. Sci. 2019, 9, 2920; doi:10.3390/app9142920

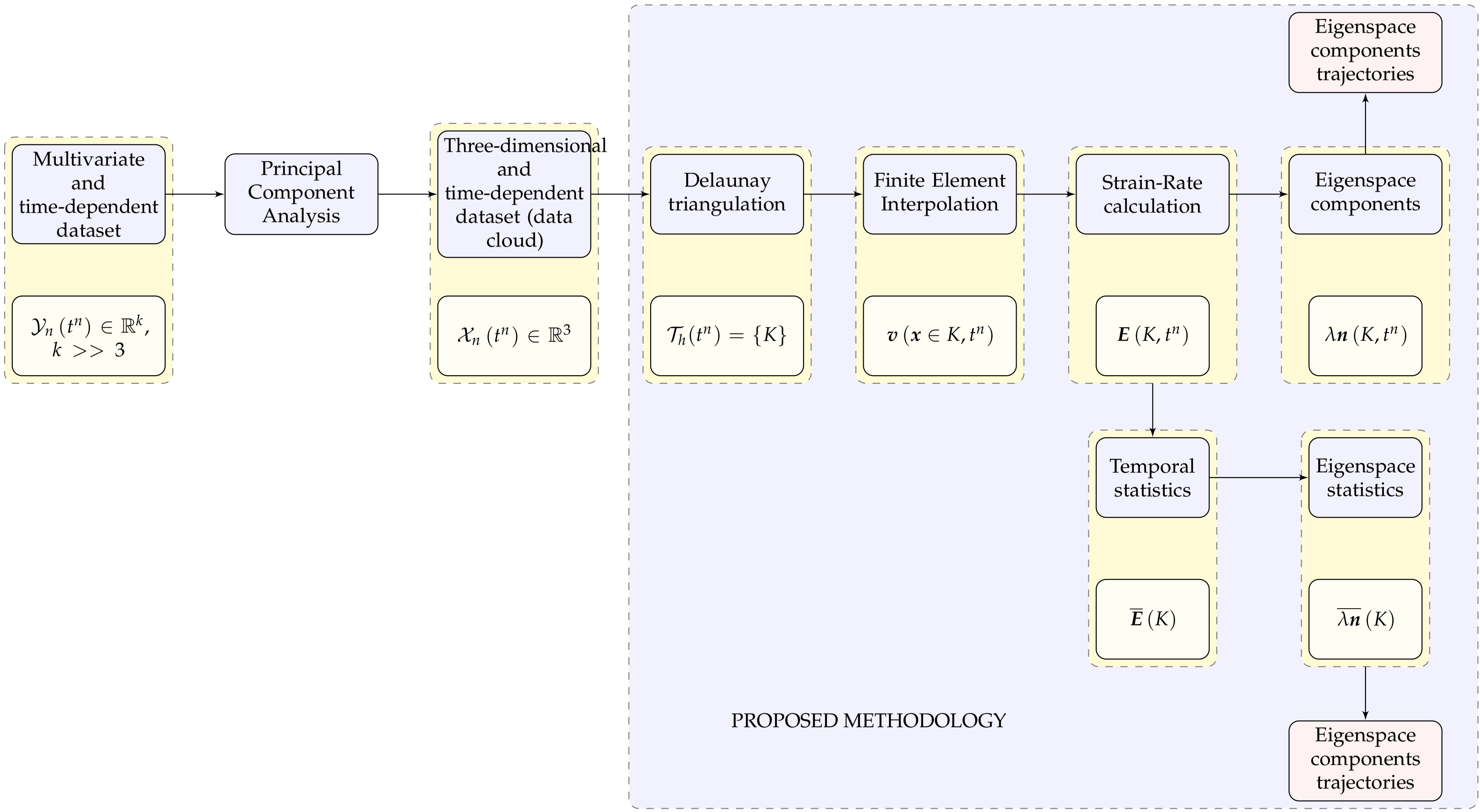

Figure 1. Flow chart of the visualization methodology.

Preprints (www.preprints.org) | NOT PEER-REVIEWED | Posted: 13 June 2019 doi:10.20944/preprints201906.0114.v1

Peer-reviewed version available at Appl. Sci. 2019, 9, 2920; doi:10.3390/app9142920

points in a certain time t. Let us consider a uniform partition of the time interval in which the dataset $\mathcal{X}_n(t)$ is defined $t \in [t^d, t^g]$ in a sequence of discrete time-steps $t^d = t^0 < t^1 < \ldots < t^n < \ldots < t^N = t^g$, with $\delta t > 0$ the time-step-size defining $t^{n+1} = t^n + \delta t$ for $n = 0, 1, 2, ..., N$. Thereby, we use the superscripts to denote the discrete time-steps, with the only exception of denoting the transpose operation with the superscript $\top$.

Since the time-dependent dataset of the case study comes from a PCA reduction of a higher-dimensional multivariate dataset $\mathcal{Y}_n(t) = \{\boldsymbol{y}_1(t), \boldsymbol{y}_2(t), \ldots, \boldsymbol{y}_i(t), \ldots, \boldsymbol{y}_n(t)\} \in \mathbb{R}^k$, with $k >> 3$ and $t \in [t^d, t^g]$, into a lower-dimensional one $\mathcal{X}_n(t)$, $t \in [t^d, t^g]$, that possesses only three independent dimensions: Principal Component 1 (PC1), Principal Component 2 (PC2), and Principal Component 3 (PC3), we use the Cartesian coordinate system straightforwardly with each principal component being a dimension. This is, $\boldsymbol{x}_i(t^n) = [x_{i,\text{PC1}}(t^n) \quad x_{i,\text{PC2}}(t^n) \quad x_{i,\text{PC3}}(t^n)]^\top$. Hence, the discrete time-dependent data-set can be thought as a cloud of points in the three-dimensional space that deforms gradually throughout time.

2.2. Finite Element Method interpolation

The main idea of the present approach is to transform the discrete cloud of points into a mathematical framework -similar to a deformable medium- by which the strain-rate tensor can be computed. To do so, we generate a mesh $\mathcal{T}_h(t) = \{K\}$ from the set of points $\mathcal{P}$ that is composed by non-overlapping and conforming geometrical elements K of diameter h. There are several methods to generate a mesh from a set of points, all which are studied in the computational geometry field. Here, we apply the Delaunay Triangulation $DT(\mathcal{P})$ because of several reasons. The first is that the aspect ratio of the triangulated elements produce a high-quality mesh. The second is because fast Delaunay triangulation algorithms have been developed recently (see for example the one in [35]).

The result of applying the Delaunay triangulation over the set of points is a discrete mesh $\mathcal{T}_h := DT(\mathcal{P})$ which possess the following characteristics: it covers exactly the convex hull Ω of the point set, no point p_i is isolated from the triangulation, and all the elements $\{K\}$ are 4-points tetrahedron, which are completely defined by the position of their four corner points $K := \{\boldsymbol{x}_j\}$, with $j = 1, 2, 3, 4$. The generated mesh $\mathcal{T}_h = DT(\mathcal{P})$ can be seen as a -material- domain Ω that suffers deformations from the displacements of the points between consecutive time-steps. Since only discrete displacements between consecutive time-steps are known for the set of points, we now explain how the continuous velocity field inside the mesh is calculated.

Even though the FEM has been used to perform interpolation using the point-wise data (see, for instance, [33,34]), in this work we apply this well-known method in a three-dimensional setting. In FEM, the finite interpolating space $\boldsymbol{\mathcal{V}}_h$ is defined as made of continuous piece-wise polynomials $N(\boldsymbol{x})$ in the mesh $\mathcal{T}_h$, where the discrete approximation $\boldsymbol{F}_h(\boldsymbol{x}, t) \in \boldsymbol{\mathcal{V}}_h$ of any multi-dimensional function $\boldsymbol{F}(\boldsymbol{x}, t)$, $\boldsymbol{x} \in \Omega$, can be written as

$$\boldsymbol{F}(\boldsymbol{x}, t) \approx \boldsymbol{F}_h(\boldsymbol{x}, t) := \sum_{i=1}^{n} N(\boldsymbol{x}_i)\boldsymbol{F}_i(t), \qquad \boldsymbol{x} \in \Omega. \tag{1}$$

We use the simplest finite element: the tetrahedron with *linear polynomials* and four nodes. Let us first introduce some notation in order to define the polynomials inside the element. The set of normalized coordinates $\chi_1, \chi_2, \chi_3, \chi_4$ in each tetrahedron K are such that the value of χ_i is one at the point $p_i \in K$, zero at the other three corner points, and varies linearly from that point to the opposite edges. This set of coordinates has the property that the sum of the four coordinates (each belonging to one tetrahedron point) in any location inside the tetrahedron is identically one: $\chi_1(\boldsymbol{x}_i) + \chi_2(\boldsymbol{x}_i) + \chi_3(\boldsymbol{x}_i) + \chi_4(\boldsymbol{x}_i) = 1$, with $\boldsymbol{x}_i \in K$. Hence, the shape functions inside each linear tetrahedron are defined to be these coordinates: $N_i(\boldsymbol{x}_i) = \chi_i(\boldsymbol{x}_i)$, with $i = 1, 2, 3, 4$ denoting the corner points. The FEM interpolation (1) of a *three-dimensional vector function*, say $\boldsymbol{F}(\boldsymbol{x},t)$, can be defined inside each linear tetrahedron K as

$$\boldsymbol{F}(\boldsymbol{x},t)=\chi_1(\boldsymbol{x})\,\boldsymbol{F}_1(t)+\chi_2(\boldsymbol{x})\,\boldsymbol{F}_2(t)+\chi_3(\boldsymbol{x})\,\boldsymbol{F}_3(t)+\chi_4(\boldsymbol{x})\,\boldsymbol{F}_4(t)=\sum_{j=1}^{4}\chi_j(\boldsymbol{x})\,\boldsymbol{F}_j(t)\,,\quad \boldsymbol{x}\in K, \tag{2}$$

160 by denoting $\boldsymbol{F}_i(t)=\boldsymbol{F}(\boldsymbol{x}_i,t)$, for $i=1,2,3,4$, nodes of the tetrahedron.

The way the tetrahedral coordinates χ_i, $i=1,2,3,4$, are defined is by means of the previous interpolating relation together with the summation constraint. This is, when one aims to define the tetrahedron geometry and calculate any position inside the tetrahedron $\boldsymbol{x}=\begin{bmatrix}x_1 & x_2 & x_3\end{bmatrix}^\top$, we compute

$$\begin{bmatrix}1\\x_1\\x_2\\x_3\end{bmatrix}=\begin{bmatrix}1&1&1&1\\x_{1,1}&x_{2,1}&x_{3,1}&x_{4,1}\\x_{1,2}&x_{2,2}&x_{3,2}&x_{4,2}\\x_{1,3}&x_{2,3}&x_{3,3}&x_{4,3}\end{bmatrix}\begin{bmatrix}\chi_1(\boldsymbol{x})\\\chi_2(\boldsymbol{x})\\\chi_3(\boldsymbol{x})\\\chi_4(\boldsymbol{x})\end{bmatrix}\quad\therefore\quad\begin{bmatrix}\chi_1(\boldsymbol{x})\\\chi_2(\boldsymbol{x})\\\chi_3(\boldsymbol{x})\\\chi_4(\boldsymbol{x})\end{bmatrix}=\frac{1}{6v}\begin{bmatrix}6v&a_1&b_1&c_1\\6v&a_2&b_2&c_2\\6v&a_3&b_3&c_3\\6v&a_4&b_1&c_4\end{bmatrix}\begin{bmatrix}1\\x_1\\x_2\\x_3\end{bmatrix} \tag{3}$$

in order to obtain the tetrahedral coordinates system where the coefficients of the inverted matrix are given by

$$\begin{aligned}
a_1&=x_{2,2}x_{43,3}-x_{3,2}x_{42,3}+x_{4,2}x_{32,3}, & b_1&=-x_{2,1}x_{43,3}+x_{3,1}x_{42,3}-x_{4,1}x_{32,3}, & c_1&=x_{2,1}x_{43,2}-x_{3,1}x_{42,2}+x_{4,1}x_{32,2},\\
a_2&=-x_{1,2}x_{43,3}+x_{3,2}x_{41,3}-x_{4,2}x_{31,3}, & b_2&=x_{1,1}x_{43,3}-x_{3,1}x_{41,3}+x_{4,1}x_{31,3}, & c_1&=-x_{1,1}x_{43,2}+x_{3,1}x_{41,2}-x_{4,1}x_{31,2},\\
a_3&=x_{1,2}x_{42,3}-x_{2,2}x_{41,3}+x_{4,2}x_{21,3}, & b_3&=-x_{1,1}x_{42,3}+x_{2,1}x_{41,3}-x_{4,1}x_{21,3}, & c_3&=x_{1,1}x_{42,2}-x_{2,1}x_{41,2}+x_{4,1}x_{21,2},\\
a_4&=-x_{1,2}x_{32,3}+x_{2,2}x_{31,3}-x_{3,2}x_{21,3}, & b_4&=x_{1,1}x_{32,3}-x_{2,1}x_{31,3}+x_{3,1}x_{21,3}, & c_4&=-x_{1,1}x_{32,2}+x_{2,1}x_{31,2}-x_{3,1}x_{21,2}.
\end{aligned}$$

Here, the abbreviation $\boldsymbol{x}_{ij}=\boldsymbol{x}_i-\boldsymbol{x}_j$ has been used, and the volume v can be calculated with the expression

$$6v=x_{21,1}\left(x_{31,2}x_{41,3}-x_{41,2}x_{31,3}\right)+x_{21,2}\left(x_{41,1}x_{31,3}-x_{31,1}x_{41,3}\right)+x_{21,3}\left(x_{31,1}x_{41,2}-x_{41,1}x_{31,2}\right).$$

At this point, it is possible to calculate the spatial derivatives of any interpolated function $\frac{\partial}{\partial \boldsymbol{x}}\boldsymbol{F}(\boldsymbol{x},t)$ in terms of the tetrahedral coordinates as

$$\frac{\partial \boldsymbol{F}(\boldsymbol{x},t)}{\partial \boldsymbol{x}}=\begin{bmatrix}\frac{\partial \boldsymbol{F}(\boldsymbol{x},t)}{\partial x_1}\\\frac{\partial \boldsymbol{F}(\boldsymbol{x},t)}{\partial x_2}\\\frac{\partial \boldsymbol{F}(\boldsymbol{x},t)}{\partial x_3}\end{bmatrix}=\sum_{j=1}^{4}\begin{bmatrix}\frac{\partial \boldsymbol{F}(\boldsymbol{x},t)}{\partial \chi_j}\frac{\partial \chi_j}{\partial x_1}\\\frac{\partial \boldsymbol{F}(\boldsymbol{x},t)}{\partial \chi_j}\frac{\partial \chi_j}{\partial x_2}\\\frac{\partial \boldsymbol{F}(\boldsymbol{x},t)}{\partial \chi_j}\frac{\partial \chi_j}{\partial x_3}\end{bmatrix}=\sum_{j=1}^{4}\begin{bmatrix}\frac{1}{6v}\frac{\partial \boldsymbol{F}(\boldsymbol{x},t)}{\partial \chi_j}a_j\\\frac{1}{6v}\frac{\partial \boldsymbol{F}(\boldsymbol{x},t)}{\partial \chi_j}b_j\\\frac{1}{6v}\frac{\partial \boldsymbol{F}(\boldsymbol{x},t)}{\partial \chi_j}c_j\end{bmatrix},\qquad \boldsymbol{x}\in K. \tag{4}$$

The way to calculate the continuous stress-rate tensor field is through the derivation of a continuous version of the velocities. Hence, we calculate the continuous velocity field by means of the FEM, in which linear piece-wise polynomials are used to interpolate the velocity at any spatial position inside the mesh. Let us explain how to calculate the discrete velocities of points. We suppose that the displacement $\boldsymbol{s}_i$ of point p_i in the time interval $\left(t^n,t^{n+1}\right)$ can be defined -without loss of accuracy- as infinitesimal, in the sense of $\boldsymbol{s}_i\left(t^n\right)\approx\boldsymbol{x}_i\left(t^{n+1}\right)-\boldsymbol{x}_i\left(t^n\right)$. We rely on the *Taylor* expansion:

$$\boldsymbol{x}_i(t)=\sum_{k=1}^{\infty}\frac{\delta t^k}{k!}\left.\frac{d^k\boldsymbol{x}_i}{dt^k}\right|_{t=t_o}=\boldsymbol{x}_i(t_0)+\left.\frac{d\boldsymbol{x}_i}{dt}\right|_{t=t_o}\delta t+\left.\frac{d^2\boldsymbol{x}_i}{dt^2}\right|_{t=t_o}\frac{\delta t^2}{2}+\cdots, \tag{5}$$

in order to calculate the discrete velocity $\boldsymbol{v}_i$ of point p_i as

$$\boldsymbol{v}_i\left(t^n\right)=\left.\frac{d\boldsymbol{x}_i}{dt}\right|_{t=t^n}\approx\frac{\boldsymbol{x}_i\left(t^{n+1}\right)-\boldsymbol{x}_i\left(t^n\right)}{\delta t}=\frac{\boldsymbol{x}_i\left(t^{n+1}\right)-\boldsymbol{x}_i\left(t^n\right)}{\left(t^{n+1}-t^n\right)}, \tag{6}$$

161 where the second (and higher) order terms are neglected.

Preprints (www.preprints.org) | NOT PEER-REVIEWED | Posted: 13 June 2019 doi:10.20944/preprints201906.0114.v1

Peer-reviewed version available at Appl. Sci. 2019, 9, 2920; doi:10.3390/app9142920

With the previous result in hand, we then generate a continuous version of (6) by replacing it in (2).

2.3. Elemental strain-rate calculation

Having defined the continuous space of velocities, we can calculate the derivatives along each one of the spatial directions and derive the strain-rate tensor field.

Following the continuum mechanics concepts in [15] and assuming small deformations, the *strain-rate tensor* is calculated as

$$\boldsymbol{E}\left(\boldsymbol{x},t^{n}\right) := \frac{1}{2}\left(\nabla \boldsymbol{v}\left(\boldsymbol{x},t^{n}\right) + \left(\nabla \boldsymbol{v}\left(\boldsymbol{x},t^{n}\right)\right)^{\top}\right),$$

with $\nabla \boldsymbol{v}$ the gradient of velocity. Each component of the $3\times 3-$tensor is developed in Cartesian coordiantes as

$$\begin{bmatrix} E_{11} & E_{12} & E_{13} \\ E_{21} & E_{22} & E_{23} \\ E_{31} & E_{32} & E_{33} \end{bmatrix} = \begin{bmatrix} \frac{\partial v_1(\boldsymbol{x},t^n)}{\partial x_1} & \frac{1}{2}\left(\frac{\partial v_1(\boldsymbol{x},t^n)}{\partial x_2} + \frac{\partial v_2(\boldsymbol{x},t^n)}{\partial x_1}\right) & \frac{1}{2}\left(\frac{\partial v_1(\boldsymbol{x},t^n)}{\partial x_3} + \frac{\partial v_3(\boldsymbol{x},t^n)}{\partial x_1}\right) \\ \frac{1}{2}\left(\frac{\partial v_2(\boldsymbol{x},t^n)}{\partial x_1} + \frac{\partial v_1(\boldsymbol{x},t^n)}{\partial x_2}\right) & \frac{\partial v_2(\boldsymbol{x},t^n)}{\partial x_2} & \frac{1}{2}\left(\frac{\partial v_2(\boldsymbol{x},t^n)}{\partial x_3} + \frac{\partial v_3(\boldsymbol{x},t^n)}{\partial x_2}\right) \\ \frac{1}{2}\left(\frac{\partial v_3(\boldsymbol{x},t^n)}{\partial x_1} + \frac{\partial v_1(\boldsymbol{x},t^n)}{\partial x_3}\right) & \frac{1}{2}\left(\frac{\partial v_3(\boldsymbol{x},t^n)}{\partial x_2} + \frac{\partial v_2(\boldsymbol{x},t^n)}{\partial x_3}\right) & \frac{\partial v_3(\boldsymbol{x},t^n)}{\partial x_3} \end{bmatrix}.$$

The six independent components of the strain-rate tensor can be arranged using *Voigt's* notation into a 6-component strain-rate vector as follows:

$$\boldsymbol{E}\left(\boldsymbol{x},t^{n}\right) = \begin{bmatrix} E_{11}\left(\boldsymbol{x},t^{n}\right) & E_{22}\left(\boldsymbol{x},t^{n}\right) & E_{33}\left(\boldsymbol{x},t^{n}\right) & \gamma_{12}\left(\boldsymbol{x},t^{n}\right) & \gamma_{23}\left(\boldsymbol{x},t^{n}\right) & \gamma_{31}\left(\boldsymbol{x},t^{n}\right) \end{bmatrix}^{\top} \tag{7}$$

where $\gamma_{12}\left(\boldsymbol{x},t\right) = 2E_{12}\left(\boldsymbol{x},t\right), \gamma_{23}\left(\boldsymbol{x},t\right) = 2E_{23}\left(\boldsymbol{x},t\right)$ and $\gamma_{13}\left(\boldsymbol{x},t\right) = 2E_{13}\left(\boldsymbol{x},t\right)$ are the *Shear-Rate Strains*. With this notation in hand, the strain-rate tensor can be calculated as

$$\boldsymbol{E}\left(\boldsymbol{x},t^{n}\right) = \begin{bmatrix} E_{11}\left(\boldsymbol{x},t^{n}\right) \\ E_{22}\left(\boldsymbol{x},t^{n}\right) \\ E_{33}\left(\boldsymbol{x},t^{n}\right) \\ \gamma_{12}\left(\boldsymbol{x},t^{n}\right) \\ \gamma_{23}\left(\boldsymbol{x},t^{n}\right) \\ \gamma_{31}\left(\boldsymbol{x},t^{n}\right) \end{bmatrix} = \begin{bmatrix} \frac{\partial}{\partial x_1} & 0 & 0 \\ 0 & \frac{\partial}{\partial x_2} & 0 \\ 0 & 0 & \frac{\partial}{\partial x_3} \\ \frac{\partial}{\partial x_2} & \frac{\partial}{\partial x_1} & 0 \\ 0 & \frac{\partial}{\partial x_3} & \frac{\partial}{\partial x_2} \\ \frac{\partial}{\partial x_3} & 0 & \frac{\partial}{\partial x_1} \end{bmatrix} \begin{bmatrix} v_1\left(\boldsymbol{x},t^{n}\right) \\ v_2\left(\boldsymbol{x},t^{n}\right) \\ v_3\left(\boldsymbol{x},t^{n}\right) \end{bmatrix}, \tag{8}$$

by defining the matrix operator of derivatives over the velocity field. In the case of the right hand side velocities, we can arrange a node-wise vector of discrete velocities in the tetrahedron K, as

$$\boldsymbol{V}\left(K,t^{n}\right) = \begin{bmatrix} v_{1,1}\left(t^{n}\right) & v_{1,2}\left(t^{n}\right) & v_{1,3}\left(t^{n}\right) & v_{2,1}\left(t^{n}\right) & v_{2,2}\left(t^{n}\right) & \ldots & v_{4,2}\left(t^{n}\right) & v_{4,3}\left(t^{n}\right) \end{bmatrix}^{\top}.$$

Using the definition of the finite element interpolation of any function (2) together with its partial derivatives (4), and replacing those in (8), we obtain

$$\boldsymbol{E}\left(\boldsymbol{x},t^{n}\right) = \frac{1}{6v}\sum_{j=1}^{4} \begin{bmatrix} a_j\frac{\partial}{\partial \chi_j} & 0 & 0 \\ 0 & b_j\frac{\partial}{\partial \chi_j} & 0 \\ 0 & 0 & c_j\frac{\partial}{\partial \chi_j} \\ b_j\frac{\partial}{\partial \chi_j} & a_j\frac{\partial}{\partial \chi_j} & 0 \\ 0 & c_j\frac{\partial}{\partial \chi_j} & b_j\frac{\partial}{\partial \chi_j} \\ c_j\frac{\partial}{\partial \chi_j} & 0 & a_j\frac{\partial}{\partial \chi_j} \end{bmatrix} \begin{bmatrix} \chi_j\left(\boldsymbol{x}\right)V_{j,1}\left(t^{n}\right) \\ \chi_j\left(\boldsymbol{x}\right)V_{j,2}\left(t^{n}\right) \\ \chi_j\left(\boldsymbol{x}\right)V_{j,3}\left(t^{n}\right) \end{bmatrix}. \tag{9}$$

Preprints (www.preprints.org) | NOT PEER-REVIEWED | Posted: 13 June 2019 doi:10.20944/preprints201906.0114.v1

Peer-reviewed version available at *Appl. Sci.* **2019**, *9*, 2920; doi:10.3390/app9142920

Now, the operation $\frac{\partial \chi_i}{\partial \chi_j} F_j = F_i$ since $\frac{\partial \chi_i}{\partial \chi_j} = \delta_{ij}$, with δ_{ij} the Kronecker delta. Hence, $\boldsymbol{E}(K, t^n)$ can be calculated as the product of the matrix $\mathbf{S}(K)$ and the vector $\boldsymbol{V}(K, t^n)$. This is,

$$\boldsymbol{E}(K, t^n) = \mathbf{S}(K, t^n)\, \boldsymbol{V}(K, t^n), \tag{10}$$

with $\boldsymbol{x} \in K$ and the discrete matrix $\mathbf{S}(K, t^n)$ defined as

$$\mathbf{S}(K, t^n) = \frac{1}{6v} \begin{bmatrix} a_1 & 0 & 0 & a_2 & 0 & 0 & a_3 & 0 & 0 & a_4 & 0 & 0 \\ 0 & b_1 & 0 & 0 & b_2 & 0 & 0 & b_3 & 0 & 0 & b_4 & 0 \\ 0 & 0 & c_1 & 0 & 0 & c_2 & 0 & 0 & c_3 & 0 & 0 & c_4 \\ b_1 & a_1 & 0 & b_2 & a_2 & 0 & b_3 & a_3 & 0 & b_4 & a_4 & 0 \\ 0 & c_1 & b_1 & 0 & c_2 & b_2 & 0 & c_3 & b_3 & 0 & c_4 & b_4 \\ c_1 & 0 & a_1 & c_2 & 0 & a_2 & c_3 & 0 & a_3 & c_4 & 0 & a_4 \end{bmatrix}. \tag{11}$$

Thus, this last matrix can be computed solely in terms of the coordinates of the nodes.

Up to this point, we have demonstrated how to calculate the elemental strain-rate. Now, our purpose is to identify the data cloud transformation throughout the visualization of the strain-rate patterns. This is, we need to identify the extrema strain-rates and their orientations. In a formal sense, this is the well-known *Eigenvalues and Eigenvectors* problem, which is stated as: if T is a linear transformation from a vector space V over a field F into itself, and v is a vector in V that is not the zero vector, then v is an eigenvector of T if $T(v)$ is a scalar multiple of v. Knowing that by definition the second order strain-rate tensor is a linear operator from a vector field into another first-order tensor field, the previous definition applied to the strain-rate tensor leads to:

$$[\boldsymbol{E}(K, t^n) - \boldsymbol{I}\lambda(K, t^n)]\, \boldsymbol{n}(K, t^n) = 0, \tag{12}$$

where $\boldsymbol{I}$ is the 3×3 identity tensor, $\boldsymbol{n}(K, t^n) \in \mathbb{R}^3$ is a normalized (non zero), i.e. unit, vector called eigenvector, and $\lambda(K, t^n) \in \mathbb{R}$ is the eigenvalue associated with the eigenvector. In other words, an eigenvector is a vector that changes by only a scalar factor when the strain-rate tensor is applied to it, resulting in a vector parallel to itself. By solving (12) one obtains three different eigenvalues $\lambda_1(K, t^n), \lambda_2(K, t^n), \lambda_3(K, t^n)$, and three eigenvectors $\boldsymbol{n}_1(K, t^n), \boldsymbol{n}_2(K, t^n), \boldsymbol{n}_3(K, t^n)$, associated with each eigenvalue.

The eigenvalues and eigenvectors describe the principal magnitudes and orientations of the strain-rate tensor: since the diagonal components of the strain-rate tensor $E_{11}(K, t^n), E_{22}(K, t^n)$, and $E_{33}(K, t^n)$ have different values in different reference systems, one finds with the set of eigenvalues the extreme -maximum and minimum- possible values that any of these components may take. Indeed, the maximum and minimum stress-rates -and their orientations- are related with the maximum and minimum eigenvalues. In this work, we follow the notation in which positive values for the eigenvalues represent the extension-rate and negative values represent contraction-rate. Hence, $\lambda_1(K, t^n)$ is the maximum and positive eigenvalue meaning extension-rate, $\lambda_3(K, t^n)$ is the minimum and negative eigenvalue meaning contraction-rate, and $\lambda_2(K, t^n)$ is either extension or contraction rate, but in smaller magnitude.

Hence, with the extrema strain-rates at the elemental level we can reveal the deformation trend of the data cloud, and above all, locating which regions suffer the most abrupt change in the time-span. We also propose to draw the family of curves -trajectories- that are instantaneously tangent to $\lambda_1\boldsymbol{n}_1(K, t^n), \lambda_2\boldsymbol{n}_2(K, t^n)$, and $\lambda_3\boldsymbol{n}_3(K, t^n)$ in the complete mesh Ω, and thus, illustrate the main patterns of change inside the data cloud. Note that $\lambda\boldsymbol{n}(K, t^n)$ is a composition of a vector using tensor components. Those differ in formal definition, but we use this concept merely for visualization purposes.

Preprints (www.preprints.org) | NOT PEER-REVIEWED | Posted: 13 June 2019 doi:10.20944/preprints201906.0114.v1

Peer-reviewed version available at *Appl. Sci.* **2019**, *9*, 2920; doi:10.3390/app9142920

Table 1. Tetrahedral elements derived from the Delaunay Triangulation of the set of points.

Element (id)	First Vertex	Second Vertex	Third Vertex	Fourth Vertex
1	Eixample	LesCorts	Gracia	Sarria
2	SantAndreu	Horta	SantMarti	NouBarris
3	Sants	SantAndreu	SantMarti	NouBarris
4	LesCorts	Eixample	Sants	CiutatVella
5	Gracia	SantMarti	Horta	Sarria
6	Gracia	SantMarti	Sarria	LesCorts
7	Eixample	Gracia	Sants	CiutatVella
8	CiutatVella	SantAndreu	Sants	NouBarris
9	Sarria	SantMarti	Horta	LesCorts
10	Gracia	SantAndreu	Sants	CiutatVella
11	Gracia	SantAndreu	CiutatVella	NouBarris
12	Sarria	Eixample	LesCorts	CiutatVella
13	Horta	SantAndreu	Gracia	NouBarris
14	SantAndreu	SantMarti	Horta	Gracia
15	LesCorts	Eixample	Gracia	Sants
16	LesCorts	Gracia	SantMarti	Sants
17	Gracia	SantAndreu	SantMarti	Sants

3. Results

In the present section, we demonstrate the application of this methodology to quantify the temporal change of an urban multivariate system (see Figure 3). First, we cite the case study that includes the multivariate description of the ten districts of Barcelona, and whose reduced three-dimensional data-set is used as the starting point. Then, we derive the strain-rate state of the data-set, pursuing the extension and contraction patterns visualization. Finally, we close this section with insights about the city transformation implied in the strain-rate state of the data cloud.

3.1. Time-dependent data cloud from an urban multivariate description

The time-dependent data cloud comes from the PCA output of a multivariate description of the city of Barcelona. Since 1987, the city has been divided into 10 administrative districts, which are the largest territorial units of the city and can be compared with neighborhoods in a common metropolitan area: Ciutat Vella, Eixample, Gràcia, Les Corts, Sarria, Sant Andreu, Sant Marti, Horta, Sants, and Nou Barris. Barcelona has a population of approximately 1.6 million inhabitants living in 10216 ha. The inclusion of all the 10 districts in the multivariate description has been aimed to represent the city at its overall scale and to allow comparisons between them.

The raw multivariate description -from which the PCA is calculated- comprises the data of 40 environmental, economic, and social indicators for the ten districts in the time span of $t^0 = 2003 \leq t^n \leq 2015 = t^N$, $n = 0, 1, .., 12$. Hence, the case study data cloud comes from a PCA reduction of the higher-dimensional multivariate data-set $\mathcal{Y}_n(t^n) \in \mathbb{R}^{40}$, into a lower-dimensional one $\mathcal{X}_n(t^n) \in \mathbb{R}^3$ that possesses only three independent dimensions: PC1, PC2, and PC3. The dimensionally-reduced data-set from the application of the PCA is presented in Appendix A. Hence, the three-dimensional and time-dependent data cloud is composed by the coordinates $\mathcal{X}_n(t^n)$ of the $n = 10$ total number of points p_i defined in the sequence of $N = 12$ time-steps from 2003 to 2015, with the time-step size of $\delta t = 1$ year. These points are displayed in Figure 2, where all the observations -districts each year- in the time-span are included.

As the first step of our methodology, we apply the Delaunay Triangulation (DT) to the data cloud. Specifically, we calculate the DT to the set of coordinates at each time-step $\mathcal{X}_n(t^n)$. This results in a mesh $\mathcal{T}_h(t^n)$ composed by $nel = |K|$ non-overlapping tetrahedron. Table 1 expands the resulting triangulation for year 2003, with the vertices information for the $nel = 17$ tetrahedron. Since the position $\boldsymbol{x}_i(t^n)$ of a given point p_i at a later time-step can surpass the initial tetrahedron's circumscribed sphere, we recalculate the mesh triangulation at each time step t^n, $n = 1, .., 11$.

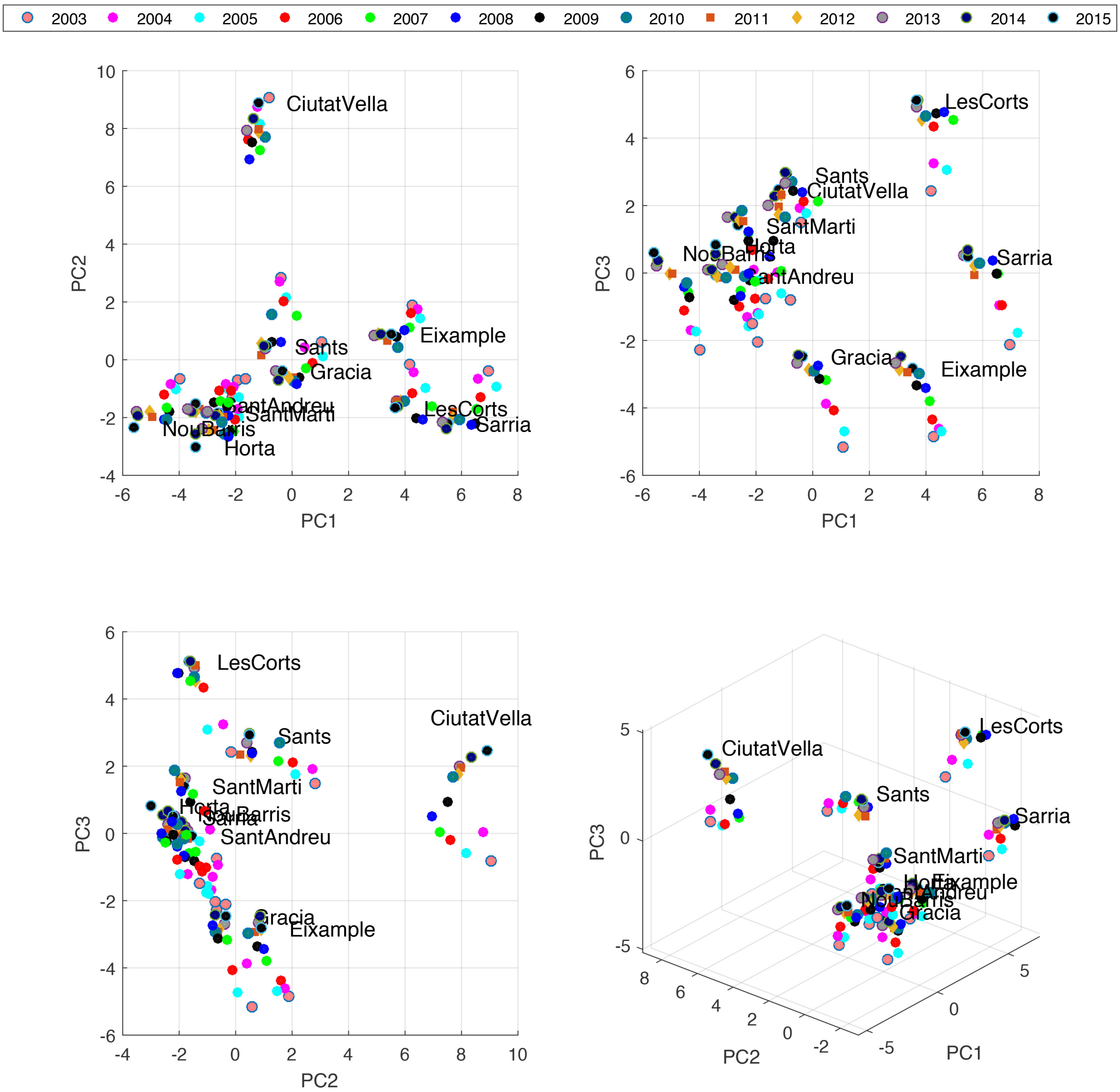

Figure 2. Three-dimensional and time-dependent data cloud from the case study.

Preprints (www.preprints.org) | NOT PEER-REVIEWED | Posted: 13 June 2019 doi:10.20944/preprints201906.0114.v1
Peer-reviewed version available at Appl. Sci. 2019, 9, 2920; doi:10.3390/app9142920

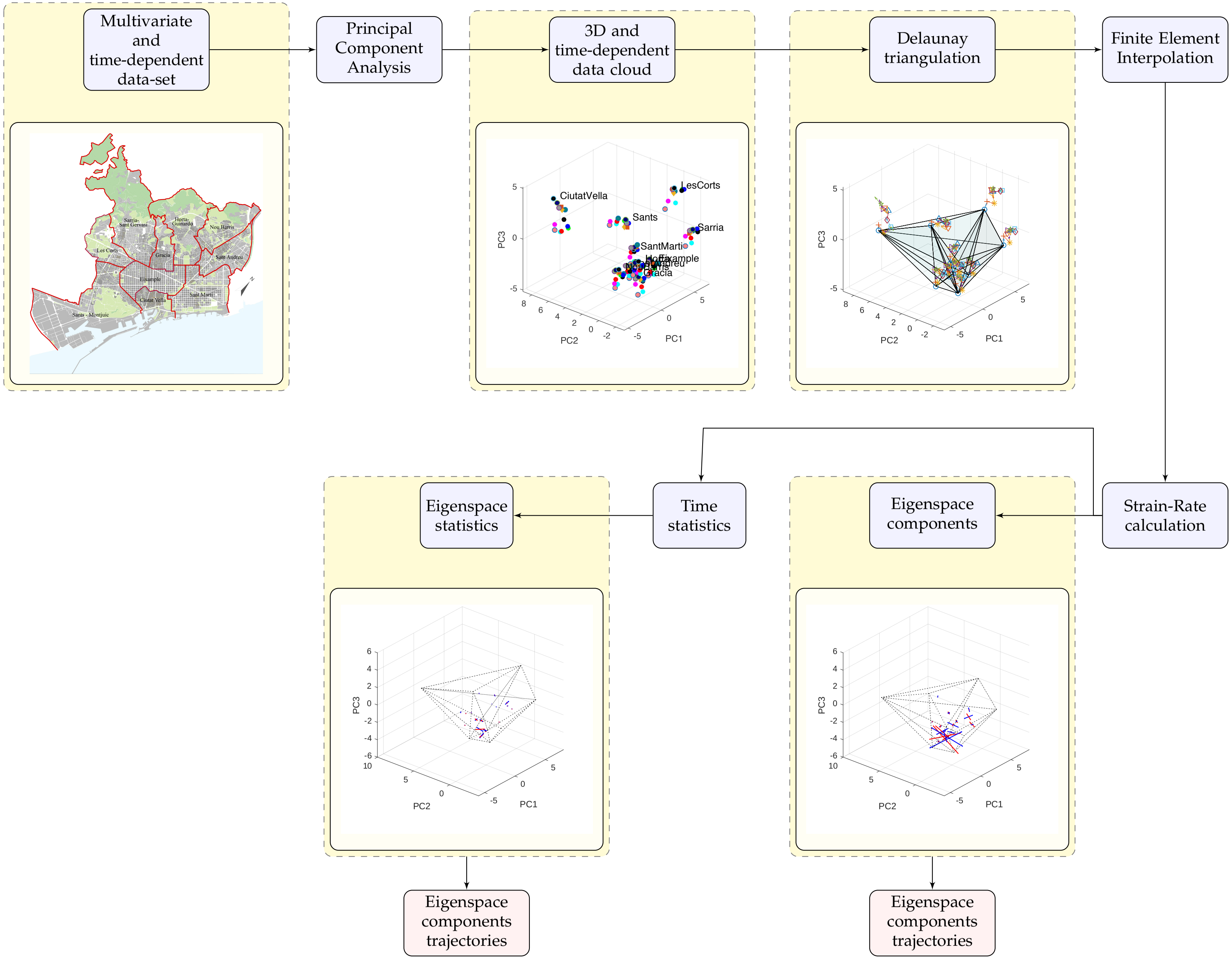

Figure 3. Flow chart of the temporal change visualization methodology.

Preprints (www.preprints.org) | NOT PEER-REVIEWED | Posted: 13 June 2019 doi:10.20944/preprints201906.0114.v1

Peer-reviewed version available at Appl. Sci. 2019, 9, 2920; doi:10.3390/app9142920

Table 2. Principal strain-rate components. Eigenvalues and Eigenvectors of the strain-rate tensor at the year 2003. The extension is denoted by the maximum eigenvalue λ_1, and contraction is denoted by the minimum eigenvalue λ_3.

Element (id)	λ_1 (year^{-1})	λ_2 (year^{-1})	λ_3 (year^{-1})	$\boldsymbol{n}_1^\top$	$\boldsymbol{n}_2^\top$	$\boldsymbol{n}_3^\top$
1	0,53152326	0,03372761	-0,5035305	[-0.4030 -0.7620 0.5069]	[-0.8521 0.1104 -0.5116]	[0.3339 -0.6381 -0.6938]
2	0,82703046	-0,07233917	-3,26208499	[0.0599 0.4379 0.8970]	[0.9979 -0.0488 -0.0428]	[0.0250 0.8977 -0.4399]
3	1,86537595	0,0239402	-1,26311701	[-0.2846 -0.7630 0.5804]	[0.8705 0.0479 0.4898]	[-0.4015 0.6447 0.6505]
4	0,13368209	0,03257601	-0,09645259	[0.3448 0.0267 0.9383]	[0.6847 -0.6909 -0.2320]	[0.6421 0.7225 -0.2565]
5	0,49758344	0,15637449	-0,04820077	[-0.2529 0.9667 0.0396]	[-0.3025 -0.1179 0.9458]	[0.9190 0.2272 0.3223]
6	0,95472589	0,0373597	-0,54006708	[-0.0595 -0.8341 0.5484]	[0.9779 0.0616 0.1998]	[-0.2005 0.5482 0.8120]
7	0,24389104	-0,02462416	-0,21220276	[0.9802 -0.0490 -0.1918]	[0.0873 0.9766 0.1964]	[0.1777 -0.2093 0.9616]
8	0,04516871	-0,00558049	-0,29509916	[-0.5143 -0.5503 -0.6578]	[0.7221 -0.6916 0.0139]	[0.4626 0.4679 -0.7531]
9	0,83841605	0,06226881	-0,72504166	[-0.4963 0.7789 0.3834]	[0.7282 0.1330 0.6723]	[-0.4727 -0.6128 0.6332]
10	0,08250367	-0,007911	-0,1849469	[-0.9511 0.1145 -0.2870]	[0.0253 -0.8969 -0.4415]	[-0.3079 -0.4272 0.8501]
11	0,1403248	-0,00962214	-0,34760551	[0.1721 -0.7223 -0.6698]	[0.9327 -0.0992 0.3467]	[0.3169 0.6844 -0.6566]
12	0,28802797	-0,02754418	-0,54411227	[-0.1025 -0.4296 -0.8972]	[0.6308 -0.7255 0.2753]	[0.7692 0.5377 -0.3453]
13	5,25376147	-0,1612729	-2,63828711	[-0.2599 -0.7733 0.5783]	[0.9210 -0.0187 0.3890]	[-0.2900 0.6338 0.7171]
14	2,58304682	0,22953554	-2,02948589	[-0.4920 0.6994 0.5184]	[0.7802 0.0900 0.6190]	[-0.3863 -0.7091 0.5900]
15	0,28104681	0,05995401	-0,17975011	[-0.6611 -0.5949 0.4572]	[-0.7488 0.4850 -0.4518]	[-0.0470 0.6410 0.7661]
16	0,12268815	0,06554156	-0,16290843	[-0.0458 0.8952 -0.4432]	[0.9468 0.1805 0.2666]	[-0.3187 0.4074 0.8559]
17	0,17492291	0,11156825	-0,27224695	[0.5895 -0.1016 0.8014]	[-0.2177 0.9354 0.2788]	[-0.7779 -0.3388 0.5292]

3.2. *Principal strain-rates*

We compute the strain-rate tensor of each tetrahedron with the interpolated version of the velocities for the case study, such that linear piece-wise polynomial functions defined inside each tetrahedron are used in the FEM interpolation. Certainly, we suppose that the velocities come from an infinitesimal analysis in which the higher order terms of the displacement are neglected. The gradients inside each tetrahedron are also considered to be constant since the polynomial functions are of first order. Applying (10), we compute the strain-rate tensor of every tetrahedron, $\boldsymbol{E}(K, t^n)$ for time-steps $n = 0, \ldots, 11$, since displacements cannot be calculated for the last year $t^{12} = 2015$. Note that the strain-rate tensor units are year^{-1} (for the case study).

We are interested in the magnitude and orientations of the principal strain-rates -extension and contraction- at the elemental level. Hence, the next step is to solve (12) and obtain the eigenspace components (eigenvalues and eigenvectors) of the strain-rate tensor. For the sake of conciseness, we list in Table 2 the results of the principal strain-rates for the year 2003 solely.

The application of this methodology to the case study is displayed graphically in Fig. 3, beginning with the map of the ten districts of Barcelona as the abstraction of the multivariate and time-dependent dataset. The three-dimensional coordinates arising from the PCA output are displayed next. We also present next the triangulated mesh at the initial year 2003, where kinematic depictions of the point-wise displacements following (6) are plot as velocity vectors. It is clear from the visual inspection that the quantitative analysis of the temporal transformation is greatly justified, so that we calculate the strain-rate tensor over the FEM interpolation of discrete velocities and compute its principal components.

3.2.1. Trajectory patterns of the principal strain-rates

In favor of the analysis, we display the principal strain-rate components in a graphical way. One first approach is to illustrate the patterns of extension-rate and contraction-rate using a vector representation, to what is referred as the *Strain-rate diagrams* [21]. In that approach, the centroid of the tetrahedron serves as the location from which the principal components of the strain-rate tensor give a representative result inside the element. We draw the strain-rate diagram of the year 2003 in the sixth step of Fig. 3, where extension-rate is represented by symmetric blue vectors $\lambda_1 \boldsymbol{n}_1$ pointing out the centroid, and contraction-rate is represented by the red vectors $\lambda_3 \boldsymbol{n}_3$ pointing in. But, it is hard to

Preprints (www.preprints.org) | NOT PEER-REVIEWED | Posted: 13 June 2019 doi:10.20944/preprints201906.0114.v1

Peer-reviewed version available at Appl. Sci. 2019, 9, 2920; doi:10.3390/app9142920

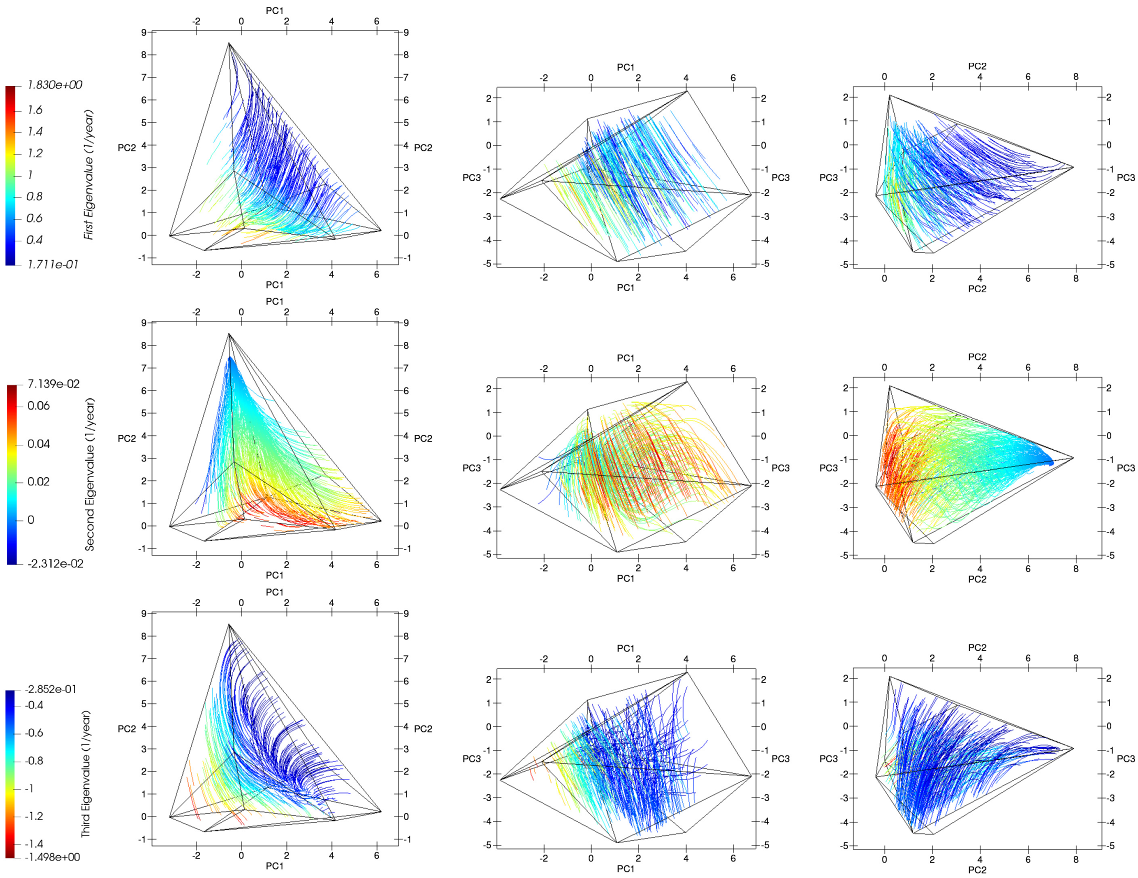

Figure 4. The trajectory patterns of the principal strain-rates at the year 2003. First principal strain-rate (top), second principal strain-rate (middle), and third principal strain-rate (bottom).

Peer-reviewed version available at Appl. Sci. 2019, 9, 2920; doi:10.3390/app9142920

visualize the distribution of the principal strain-rates and their three-dimensional orientations using this type of illustration.

Our approach to ease the visualization and understanding of the strain-rate state is to draw the *trajectories* of the principal strain-rate components, as used for displaying stresses in beams and columns in [36]. In the following we demonstrate our findings of the strain-rate state at the year 2003 using the trajectories visualization. In Figure 4 we display the principal components trajectories, where the lines are colored by the magnitude of the principal strain-rate and those are parallel to its orientation. From these representations, we can understand the magnitude and orientation of each principal component of the strain-rate tensor. And more importantly, the trajectory patterns overlapped with the coordinates of the districts (in Figure 2) provide information about local regions of extension and contraction rates inside the urban description, where extension-rate patterns means differentiation and contraction-rate patterns means clustering -or homogenization-.

In the case of the first strain-rate component which is shown at the top of Fig 4, we observe that the larger magnitude of extension-rate is localized in between Nou Barris Sant Andreu, Sant Marti, Horta and Sants, and that it decreases near Eixample, Les Corts, and Ciutat Vella. Therefore, the main transformation is located at the first cluster of districts: Nou Barris, Sant Andreu, Sant Marti, and Horta. The extension-rate patterns are oriented from this cluster apart to Ciutat Vella, suggesting that there is a divergence of Ciutat Vella from the clustered districts. Indeed, the main extension pattern is oriented along the PC3 dimension and covers the clustered districts. It is of lesser importance the pattern which comprises the districts of Nou Barris, Sant Marti, and Sants and ends at Gracia and Eixample.

Contraction-rate, on the other hand, is expressed by the third principal strain-rate component, which by definition is orthogonal to the first and second principal strain-rates. The third principal strain-rate component is shown at the bottom of Fig. 4, where we can appreciate this orthogonality by noticing that the trajectories of the third principal strain-rate are perpendicular to the extension-rate pattern. We observe that the contraction-rate trajectories are mostly homogeneous, with a minor importance between Sant Marti, Sant Andreu, Nou Barris and Horta districts, and completely declining at Sants and Gracia. This direct relation between extension and contraction is found in solids deformations, where it is ruled by the conservation of mass -or Poisson ratio- [15].

Apart from the extension and contraction patterns of the mesh, locations of smaller strain-rates are represented by the second principal component. Considering the middle plots of Fig. 4, we recognize that the orientation of this strain-rate component is concentrated in between Les Corts, Sarria, Horta and Nou Barris, and that it is directed towards Eixample, fading at Ciutat Vella. This principal strain-rate component is certainly orthogonal to the first and second components, but it implies a strain-rate pattern that is two orders of magnitude smaller.

In the previous lines we have demonstrated the application of the trajectories diagrams of the principal strain-rate components as a powerful visualization technique of the three-dimensional strain-rate state of a data cloud. The strain-rate patterns can be used to analyze the system's development, in example, with the identification of regions with a special behavior: although there are some clustered districts in the case study, all of those are separating at a high rate in dimensions 1 and 3. Hence, those are differentiating themselves in the PC1 and PC3 description. On the contrary, low strain-rates can be an indication of stagnation, and thus, an expression of inactivity where an abrupt change is not probably to occur. That is specially the case of the Ciutat Vella district, which is separated from the clustered nodes but it is neither diverging nor converging to them.

One final remark to the visualization of strain-rate patterns is that the principal strain-rate trajectory plots are mesh independent: different triangulations will produce different positions, magnitudes and orientations of the principal strain-rate components, nevertheless, trajectory lines coincide for all of them.

Preprints (www.preprints.org) | NOT PEER-REVIEWED | Posted: 13 June 2019 doi:10.20944/preprints201906.0114.v1

Peer-reviewed version available at Appl. Sci. 2019, 9, 2920; doi:10.3390/app9142920

Table 3. Time-averaged eigenspace components.

Element(id)	$\overline{\lambda_1}$ (year^{-1})	$\overline{\lambda_2}$ (year^{-1})	$\overline{\lambda_3}$ (year^{-1})	$\boldsymbol{n}_1^\top \implies \overline{\lambda_1}$	$\boldsymbol{n}_2^\top \implies \overline{\lambda_2}$	$\boldsymbol{n}_3^\top \implies \overline{\lambda_3}$
1	0,1157	-0,0086	-0,0687	[-0.4941 -0.4365 0.7519]	[0.1770 0.1339 -0.9751]	[0.1682 0.8390 0.5175]
2	0,5087	-0,0085	-0,8859	[-0.5777 0.5570 0.5966]	[-0.4259 -0.1592 -0.8907]	[-0.0636 -0.9309 0.3596]
3	0,3919	-0,0440	-0,1662	[-0.3746 -0.7054 0.6017]	[-0.9963 0.0335 0.0789]	[0.3127 -0.7926 -0.5234]
4	0,0868	0,0041	-0,0193	[0.4684 0.8217 0.3247]	[-0.0619 0.3756 -0.9247]	[-0.7437 -0.4144 -0.5246]
5	0,0435	-0,0326	-0,0659	[-0.2319 0.8799 0.4148]	[-0.0891 -0.1728 0.9809]	[0.2229 -0.2816 -0.9333]
6	0,1834	0,0096	-0,0536	[-0.2271 -0.8440 0.4859]	[-0.6281 0.2260 -0.7446]	[-0.4216 0.8544 0.3038]
7	0,0647	-0,0059	-0,0485	[0.5157 -0.6416 0.5678]	[0.0741 -0.9932 0.0893]	[0.2985 -0.4332 -0.8504]
8	0,1436	-0,0198	-0,0174	[-0.3994 -0.4110 0.8194]	[-0.1094 0.9614 -0.2525]	[0.3984 -0.8684 -0.2952]
9	0,6311	0,0178	-0,1144	[-0.2472 -0.6917 0.6785]	[0.2277 0.2955 0.9278]	[0.1771 0.8523 0.4921]
10	0,0355	0,0098	-0,0745	[0.4275 0.8923 -0.1449]	[0.8566 -0.5130 -0.0551]	[-0.5198 0.2220 -0.8249]
11	0,0452	-0,0239	-0,1039	[0.4742 -0.0948 0.8753]	[-0.7018 -0.6930 0.1650]	[-0.3132 -0.9345 -0.1693]
12	0,2054	0,0336	-0,0703	[-0.5086 -0.8385 -0.1954]	[0.1867 0.6566 0.7307]	[0.0460 -0.4726 -0.8801]
13	1,1642	-0,0218	-0,3192	[-0.4080 -0.6299 0.6609]	[-0.9632 0.2605 0.0654]	[-0.5136 0.5798 -0.6325]
14	0,1923	0,0415	-0,2640	[-0.4758 0.8168 0.3264]	[0.9570 0.2693 -0.1076]	[0.4308 -0.2715 -0.8606]
15	0,0552	0,0085	-0,0363	[-0.2364 0.6160 0.7514]	[0.7518 0.2783 -0.5978]	[0.6817 0.6544 -0.3270]
16	0,0438	0,0175	-0,0059	[0.2794 0.9257 -0.2549]	[0.8449 -0.2441 0.4760]	[-0.5430 -0.2892 -0.7883]
17	0,2113	-0,0196	-0,3129	[-0.0062 0.9656 0.2599]	[0.0760 0.2441 0.9668]	[0.0666 -0.9959 -0.0609]

Table 4. Maximum and minimum eigenspace components in the time span.

Element(id)	$L^\infty(\lambda_1)$	Year	$\boldsymbol{n}_1^\top \implies L^\infty(\lambda_1)$	$L^{-\infty}(\lambda_3)$	Year	$\boldsymbol{n}_3^\top \implies L^{-\infty}(\lambda_3)$
1	0,5315	2003	[-0.4030 -0.7620 0.5069]	-0,5035	2003	[0.3339 -0.6381 -0.6938]
2	2,0893	2010	[-0.5094 0.8338 0.2130]	-3,2621	2003	[0.0250 0.8977 -0.4399]
3	3,0249	2009	[-0.0766 -0.8956 0.4383]	-1,2631	2003	[-0.4015 0.6447 0.6505]
4	0,4860	2010	[0.5309 0.8024 0.2724]	-0,1901	2005	[0.8017 0.5583 -0.2134]
5	0,6321	2014	[0.0691 0.9893 -0.1286]	-0,3019	2010	[-0.3219 0.5283 0.7857]
6	1,1842	2006	[0.1651 -0.9360 0.3110]	-0,9833	2005	[0.2453 -0.7335 -0.6338]
7	0,2772	2010	[0.0108 -0.9360 0.3518]	-0,2122	2003	[0.1777 -0.2093 0.9616]
8	0,5104	2010	[-0.4614 -0.6584 0.5946]	-0,5374	2009	[-0.2484 -0.6025 0.7585]
9	4,3858	2010	[-0.2509 -0.6991 0.6696]	-2,4530	2010	[0.4203 -0.7018 -0.5752]
10	0,3753	2010	[-0.4800 0.8570 -0.1874]	-0,3477	2009	[0.4401 -0.6943 0.5695]
11	0,5210	2009	[-0.0542 0.3205 0.9457]	-0,5164	2009	[0.3738 0.8847 -0.2784]
12	1,5272	2008	[-0.6804 -0.7328 0.0027]	-0,7379	2007	[0.4304 0.8624 -0.2666]
13	5,2538	2003	[-0.2599 -0.7733 0.5783]	-4,6094	2008	[0.2022 -0.9445 0.2588]
14	2,5830	2003	[-0.4920 0.6994 0.5184]	-2,0295	2003	[-0.3863 -0.7091 0.5900]
15	0,2810	2003	[-0.6611 -0.5949 0.4572]	-0,4221	2010	[0.0927 -0.9519 -0.2919]
16	0,2659	2009	[0.4571 0.7618 -0.4591]	-0,1636	2012	[-0.5501 0.7352 0.3961]
17	1,4269	2009	[-0.0935 0.9952 0.0288]	-1,1715	2010	[0.1262 0.9888 0.0798]

Peer-reviewed version available at *Appl. Sci.* **2019**, *9*, 2920; doi:10.3390/app9142920

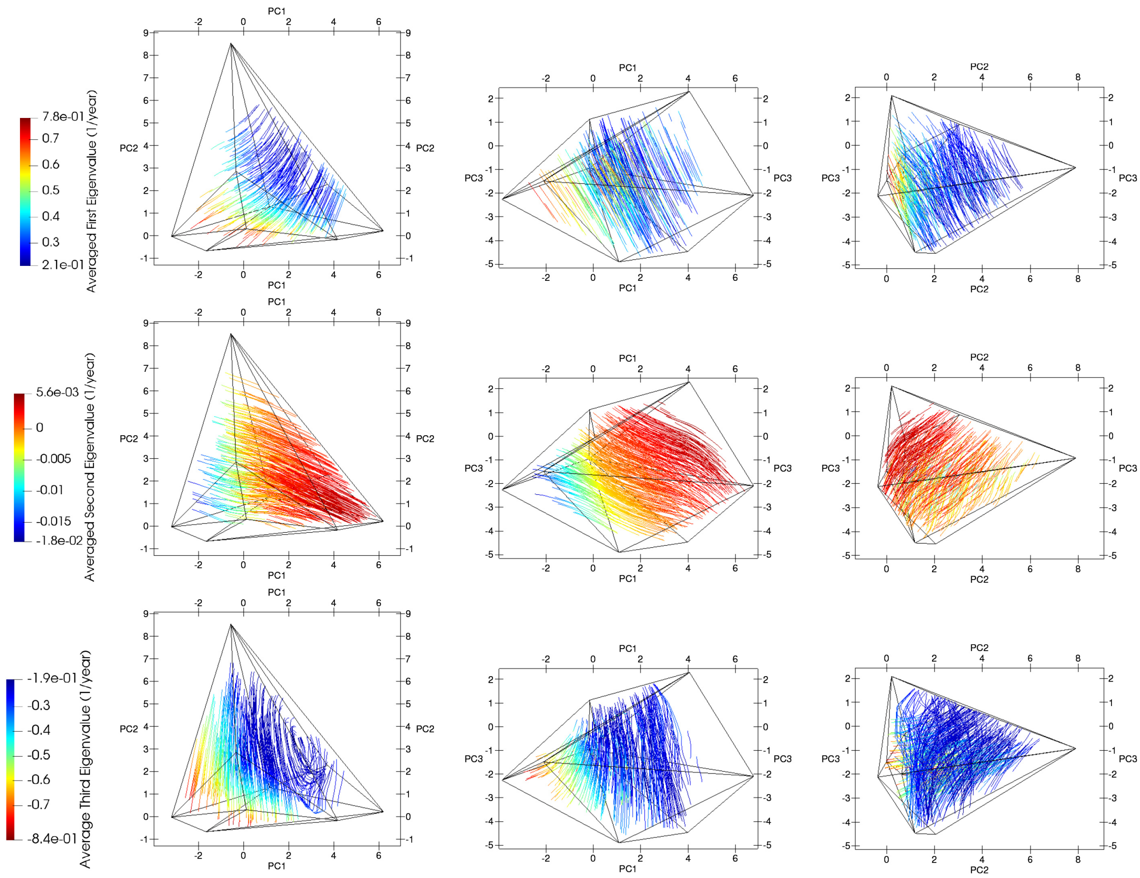

Figure 5. The trajectory patterns of the time-averaged principal strain-rates. Averaged first principal strain-rate (top), averaged second principal strain-rate (middle), and averaged third principal strain-rate (bottom).

Preprints (www.preprints.org) | NOT PEER-REVIEWED | Posted: 13 June 2019 doi:10.20944/preprints201906.0114.v1

Peer-reviewed version available at Appl. Sci. 2019, 9, 2920; doi:10.3390/app9142920

3.3. Temporal statistics of the principal strain-rates

Plots of the principal strain-rate components trajectories can be completed for the remaining years of the time span, t^n, $n = 1, 2, ..., 11$, and those are attached as meta-data in the electronic version of the present article. Readings of the strain-rate streamline patterns for those years can be completed straightforwardly as discussed in the paragraphs above. Nevertheless, we perform some temporal statistics of the strain-rate states, where the principal strain-rates calculated for each time-step are accounted as the temporal events: each strain-rate state is accounted as a single observation.

The first statistics that we perform is the time-average of the principal strain-rate components, separated as the first, second, and third principal strain-rates. Table 3 presents the time-averaged results of the principal strain-rates. Also, in the last schematic of Fig. 3, we plot the strain-rate diagram of the time-averaged principal strain-rates at the time-averaged centroid of tetrahedron elements. This figure gives insights about the orientation and magnitude of the first and third principal strain-rates, again by plotting the symmetric arrows pointing out for extension and pointing in for contraction. We complete our analysis by drawing the trajectory curves of those time-averaged strain-rate diagrams in Fig. 5.

With the aid of Figures 2 and 5 we analyze the trajectory patterns of the time-averaged strain-rate state of the data cloud. In the case of the first and third strain-rate components, those are comparable to the ones described in the previous paragraphs for the year 2003. We observe a high extension-rate behavior between Nou Barris, Sant Andreu and Horta in the PC1 dimension. The contraction-rate, on the other side, is oriented in the PC2 dimension and it is mostly located in between Gracia and Eixample and decreases near Sants. In the case of the contraction-rate in the PC3 dimension, it is mostly present between Nou Barris and Horta, and in smaller magnitude between Horta and Sant Andreu. The contraction-rate between the remaining districts is negligible in all dimensions. Both the extension and contraction rates demonstrate trajectory patterns which are directed from the clustered districts towards the separated district of Ciutat Vella. However, the magnitude of the time-averaged strain-rates is much smaller than the ones obtained for year 2003. In the case of the time-averaged second strain-rate, its magnitude is greater for Eixample, Les Corts, and Sarria nodes than for the clustered nodes. The orientation of the trajectories involving this second strain-rate component is parallel to the one linking Eixample and Les Corts to the clustered nodes.

The second temporal statistics that we perform is to calculate $L^\infty-$norm of the temporal strain-rate distribution. That is, to calculate the year where the maximum extension and contraction rates occur within each tetrahedron. The results of the application of the $L^\infty-$norm to the case study are presented in Table 4. We observe that the maximum strain-rates occur at year 2003: either expansion or contraction. Also, that important contraction-rate magnitudes take place between the years 2003 and 2010. This is not the case of the extension-rate magnitudes, which are more prevalent after year 2008.

4. Conclusions

In the present article, we have quantified the temporal change of a time-dependent and three-dimensional dataset. Contrary to other approaches [1], we have calculated the three-dimensional strain-rate state of the dataset based on the interpolation of discrete point-wise displacements -or data variations-. We have applied a technique in continuum mechanics using a FEM interpolation of non-overlapping linear tetrahedral elements that spans the three-dimensional dataset.

The methodology has demonstrated to exhibit regions of major deformation-rate. Departing from the calculation of the numerical strain-rate values, we have introduced some data-visualization techniques that help to locate the magnitudes and orientations of the strain-rate state in the three-dimensional framework. This is the case of the principal strain-rate trajectories, whose have demonstrated to be more detailed than other possible visualization techniques, e.g. strain-rate diagrams in [24,28]. The main difference with strain-rate diagrams is the ability of the former to visualize a continuum version of the strain-rate inside the dataset, and to separate the analysis into each principal component of the strain-rate state, while being mesh independent.

Peer-reviewed version available at *Appl. Sci.* **2019**, *9*, 2920; doi:10.3390/app9142920

The calculation of the strain-rate state shows that the methodology is suitable for quantifying the temporal change of a reduced three-dimensional dataset describing the social, economic and environmental state of the city of Barcelona. In particular, high strain-rates are associated with the localized deformation of regions that represent the districts of the city in the time span of 13 years. It is similar to *Cluster Analysis* [37–39] or *Distance measures* [40], in the sense that the method portrays the similarities and differences between the districts of the city. The distinctive attribute of the present work is the feasibility to quantify the districts' differentiation with time: the strain-rate tensor provides quantitative information about local regions of extension and contraction, where extension-rate patterns means differentiation and contraction-rate patterns means clustering -or homogenization-. Conclusions about the divergence or clustering of districts in time can therefore be stated. For example, it reveals the time, location, and orientation of pressures affecting the inhabitants of certain districts of the city, essentially those which are rapidly diverging from the rest (e.g. the case of Ciutat Vella for the case study). This methodology locates regions where detailed action is necessary, as well as the foretelling of possible ruptures in the system.

Finally, we would like to say that this method is not limited to the study of the data change, but can also be applied to other descriptions: a natural sequel to the present article is the study of the time-dependent data cloud as a deforming elastic solid under equilibrium. Solving the inverse problem, namely the identification of the constitutive moduli of the deforming material emerges as the first step for predicting the system's future state given its historical data.

Author Contributions: The authors equally contributed to the elaboration of this article.

Funding: This research received no external funding.

Acknowledgments: Lorena Salazar-Llano greatly acknowledges the financial support received by the pre-doctoral grant "Beca Rodolfo Llinás para la promoción de la formación avanzada y el espíritu científico de Bogotá" from Fundación CEIBA.

Conflicts of Interest: The authors declare no conflict of interest.

Appendix A

References

1. Fuchs, R.; Hauser, H. Visualization of multi-variate scientific data. Computer Graphics Forum. Wiley Online Library, 2009, Vol. 28, pp. 1670–1690.
2. Salazar-Llano, L.; Rosas-Casals, M.; Ortego, M.I. An Exploratory Multivariate Statistical Analysis to Assess Urban Diversity. *Sustainability* **Submitted**.
3. White, F.M.; Corfield, I. *Viscous fluid flow*; Vol. 3, McGraw-Hill New York, 2006.
4. Bower, A.F. *Applied mechanics of solids*; CRC press, 2009.
5. McLoughlin, T.; Laramee, R.S.; Peikert, R.; Post, F.H.; Chen, M. Over two decades of integration-based, geometric flow visualization. Computer Graphics Forum. Wiley Online Library, 2010, Vol. 29, pp. 1807–1829.
6. Süßmuth, J.; Winter, M.; Greiner, G. Reconstructing animated meshes from time-varying point clouds. Computer Graphics Forum. Wiley Online Library, 2008, Vol. 27, pp. 1469–1476.
7. Ustinin, M.N.; Kronberg, E.; Filippov, S.V.; Sytchev, V.V.; Sobolev, E.V.; Llinás, R. Kinematic visualization of human magnetic encephalography. **2010**, *5*, 176–187.
8. Wang, S.W.; Interrante, V.; Longmire, E. Multivariate visualization of 3D turbulent flow data. Visualization and Data Analysis 2010. International Society for Optics and Photonics, 2010, Vol. 7530, p. 75300N.
9. Kohler, M.; Krzyżak, A. Nonparametric estimation of non-stationary velocity fields from 3D particle tracking velocimetry data. *Computational Statistics & Data Analysis* **2012**, *56*, 1566–1580.
10. Aguirre-Pablo, A.; Aljedaani, A.B.; Xiong, J.; Idoughi, R.; Heidrich, W.; Thoroddsen, S.T. Single-camera 3D PTV using particle intensities and structured light. *Experiments in Fluids* **2019**, *60*, 25.
11. Keim, D.A. Information visualization and visual data mining. *IEEE transactions on Visualization and Computer Graphics* **2002**, *8*, 1–8.

Preprints (www.preprints.org) | NOT PEER-REVIEWED | Posted: 13 June 2019 doi:10.20944/preprints201906.0114.v1

Peer-reviewed version available at Appl. Sci. 2019, 9, 2920; doi:10.3390/app9142920

Table A1. Coordinates (seen as the component loadings of the PCA analysis) for the ten districts in the temporal span.

	Ciutat Vella			Eixample			Gracia		
Year	PC1	PC2	PC3	PC1	PC2	PC3	PC1	PC2	PC3
2003	-0,8063	9,0563	-0,8014	4,2613	1,8666	-4,832	1,05	0,6006	-5,1456
2004	-1,2263	8,749	0,0207	4,444	1,7361	-4,6018	0,4589	0,4104	-3,8634
2005	-1,1214	8,1463	-0,5941	4,538	1,4541	-4,6755	1,105	0,0923	-4,7119
2006	-1,5671	7,6138	-0,1879	4,2079	1,6011	-4,3598	0,7275	-0,1042	-4,0577
2007	-1,1198	7,2281	0,0579	4,1476	1,0994	-3,7909	0,4875	-0,305	-3,1769
2008	-1,5106	6,9424	0,4942	3,9782	1,0165	-3,4243	0,1741	-0,8197	-2,7533
2009	-1,3956	7,5225	0,9368	3,685	0,7901	-3,3483	0,2523	-0,6319	-3,1446
2010	-0,9735	7,7025	1,6649	3,7625	0,4337	-2,9882	0,0594	-0,7371	-2,9213
2011	-1,2043	7,9648	1,9629	3,3624	0,6786	-2,9333	0,0113	-0,6152	-2,9398
2012	-1,195	7,8653	1,7417	3,0545	0,9032	-2,8587	-0,1365	-0,5935	-2,8493
2013	-1,5913	7,9264	1,9916	2,9124	0,8291	-2,6614	-0,5758	-0,3804	-2,6808
2014	-1,3629	8,3386	2,2818	3,1193	0,867	-2,4646	-0,4876	-0,7186	-2,4188
2015	-1,2049	8,9012	2,4749	3,5172	0,8941	-2,8168	-0,3677	-0,3717	-2,4571

	Horta			Les Corts			Nou Barris		
Year	PC1	PC2	PC3	PC1	PC2	PC3	PC1	PC2	PC3
2003	-2,1138	-1,2904	-1,4894	4,1613	-0,1746	2,4413	-3,9792	-0,6683	-2,2832
2004	-1,9348	-1,6926	-1,2007	4,2907	-0,4407	3,246	-4,3116	-0,8449	-1,6886
2005	-1,9037	-1,9865	-1,2151	4,72	-0,9836	3,0771	-4,1319	-1,0375	-1,7496
2006	-2,0135	-2,068	-0,7788	4,2483	-1,1456	4,3327	-4,5379	-1,1949	-1,1161
2007	-2,0524	-2,4994	-0,2639	4,9414	-1,5988	4,5201	-4,4199	-1,6649	-0,5806
2008	-2,2745	-2,6368	-0,0178	4,6463	-2,081	4,7669	-4,5522	-2,0702	-0,4074
2009	-2,203	-2,4633	-0,2194	4,3805	-2,0041	4,7494	-4,3531	-1,8088	-0,7178
2010	-2,3921	-2,5868	-0,1021	3,9936	-1,4523	4,6517	-4,4486	-2,0712	-0,3091
2011	-2,751	-2,4149	0,1039	3,6955	-1,41	4,9955	-4,9566	-1,9717	-0,0125
2012	-2,94	-2,4159	0,1586	3,8331	-1,4371	4,5223	-5,0669	-1,7986	-0,0275
2013	-3,1722	-2,3885	0,2543	3,6767	-1,4507	4,9202	-5,5219	-1,7744	0,214
2014	-3,4071	-2,5664	0,5601	3,7339	-1,6226	5,1188	-5,4769	-1,9184	0,3528
2015	-3,4105	-3,0084	0,8318	3,6617	-1,6611	5,1225	-5,5952	-2,3473	0,6067

	Sant Andreu			Sant Marti			Sants		
Year	PC1	PC2	PC3	PC1	PC2	PC3	PC1	PC2	PC3
2003	-1,9206	-0,7244	-2,038	-1,6692	-0,6515	-0,759	-0,4118	2,8214	1,4929
2004	-2,3282	-0,8237	-1,2921	-2,0666	-0,9143	0,1126	-0,4382	2,7054	1,9119
2005	-2,2532	-1,0002	-1,5723	-1,8884	-1,2945	-0,2293	-0,2215	2,1389	1,7699
2006	-2,5938	-1,0519	-1,0073	-2,1435	-1,0797	0,6638	-0,321	2,0008	2,104
2007	-2,5244	-1,4196	-0,5319	-2,2487	-1,4918	1,1851	0,1661	1,5314	2,1307
2008	-2,5551	-1,8275	-0,6822	-2,2779	-1,9199	1,2394	-0,3843	0,6045	2,3897
2009	-2,772	-1,4689	-0,812	-2,2868	-1,6089	0,9544	-0,7046	0,5952	2,4362
2010	-3,0476	-1,8197	-0,1474	-2,4825	-2,1435	1,8678	-0,7341	1,5812	2,6913
2011	-3,2915	-1,7145	-0,1452	-2,4366	-1,9662	1,5397	-1,0958	0,1433	2,3358
2012	-3,3955	-1,8174	-0,1092	-2,5843	-1,9311	1,5931	-1,0935	0,5496	2,3024
2013	-3,7081	-1,7173	0,0948	-3,0101	-1,7819	1,6588	-0,961	0,3743	2,6883
2014	-3,5488	-1,8093	0,0797	-2,732	-1,9099	1,6373	-0,9836	0,4766	2,9893
2015	-3,4406	-1,5402	-0,0642	-2,6473	-1,8349	1,4236	-0,9148	0,4841	2,9255

	Sarria		
Year	PC1	PC2	PC3
2003	6,9446	-0,3658	-2,1205
2004	6,6038	-0,6365	-0,9552
2005	7,2135	-0,9469	-1,7803
2006	6,6584	-1,2802	-0,9586
2007	6,5343	-1,7212	-0,0213
2008	6,3394	-2,261	0,3627
2009	6,4824	-2,2093	-0,0221
2010	5,9119	-2,0589	0,2891
2011	5,7193	-1,7978	-0,0559
2012	5,716	-2,0188	0,2245
2013	5,3182	-2,1666	0,5166
2014	5,4857	-2,3904	0,6632
2015	5,4919	-2,1922	0,4949

12. Gao, L.; Heath, D.G.; Kuszyk, B.S.; Fishman, E.K. Automatic liver segmentation technique for three-dimensional visualization of CT data. *Radiology* **1996**, *201*, 359–364.
13. Teplan, M.; others. Fundamentals of EEG measurement. *Measurement science review* **2002**, *2*, 1–11.
14. Wang, C.; Yu, H.; Ma, K.L. Importance-driven time-varying data visualization. *IEEE Transactions on Visualization and Computer Graphics* **2008**, *14*, 1547–1554.
15. Mase, G.T.; Smelser, R.E.; Mase, G.E. *Continuum mechanics for engineers*; CRC press, 2009.
16. Marsden, J.E.; Hughes, T.J. *Mathematical foundations of elasticity*; Courier Corporation, 1994.
17. Xu, P.; Grafarend, E. Statistics and geometry of the eigenspectra of three-dimensional second-rank symmetric random tensors. *Geophysical Journal International* **1996**, *127*, 744–756.
18. Wdowinski, S.; Sudman, Y.; Bock, Y. Geodetic detection of active faults in S. California. *Geophysical research letters* **2001**, *28*, 2321–2324.
19. Straub, C.; Kahle, H.G.; Schindler, C. GPS and geologic estimates of the tectonic activity in the Marmara Sea region, NW Anatolia. *Journal of Geophysical Research: Solid Earth* **1997**, *102*, 27587–27601.
20. Moin, P. *Fundamentals of engineering numerical analysis*; Cambridge University Press, 2010.
21. Hackl, M.; Malservisi, R.; Wdowinski, S. Strain rate patterns from dense GPS networks. *Natural Hazards and Earth System Sciences* **2009**, *9*, 1177–1187.
22. Wang, H.; Amini, A.A. Cardiac motion and deformation recovery from MRI: A review. *IEEE Transactions on Medical Imaging* **2012**, *31*, 487–503.
23. Pedrizzetti, G.; Sengupta, S.; Caracciolo, G.; Park, C.S.; Amaki, M.; Goliasch, G.; Narula, J.; Sengupta, P.P. Three-dimensional principal strain analysis for characterizing subclinical changes in left ventricular function. *Journal of the American Society of Echocardiography* **2014**, *27*, 1041–1050.
24. Cai, J.; Grafarend, E.W. Statistical analysis of geodetic deformation (strain rate) derived from the space geodetic measurements of BIFROST Project in Fennoscandia. *Journal of Geodynamics* **2007**, *43*, 214–238.
25. Cai, J.; Grafarend, E.W. Statistical analysis of the eigenspace components of the two-dimensional, symmetric rank-two strain rate tensor derived from the space geodetic measurements (ITRF92-ITRF2000 data sets) in central Mediterranean and Western Europe. *Geophysical Journal International* **2007**, *168*, 449–472.
26. Mastrolembo, B.; Caporali, A. Stress and strain-rate fields: A comparative analysis for the Italian territory. *Bollettino di Geofisica Teorica ed Applicata* **2017**, *58*.
27. Houlie, N.; Woessner, J.; Giardini, D.; Rothacher, M. Lithosphere strain rate and stress field orientations near the Alpine arc in Switzerland. *Scientific reports* **2018**, *8*.
28. Su, X.; Yao, L.; Wu, W.; Meng, G.; Su, L.; Xiong, R.; Hong, S. Crustal deformation on the northeastern margin of the Tibetan plateau from continuous GPS observations. *Remote Sensing* **2019**, *11*, 34.
29. Sneddon, I.N. The distribution of stress in the neighbourhood of a crack in an elastic solid. *Proceedings of the Royal Society of London. Series A. Mathematical and Physical Sciences* **1946**, *187*, 229–260.
30. Williams, M. The bending stress distribution at the base of a stationary crack. *Trans. ASME* **1957**, *79*, 109–114.
31. Aktuğ, B.; Parmaksız, E.; Kurt, M.; Lenk, O.; Kılıçoğlu, A.; Gürdal, M.A.; Özdemir, S. Deformation of central anatolia: GPS implications. *Journal of Geodynamics* **2013**, *67*, 78–96.
32. Grafarend, E. Criterion matrices for deforming networks. In *Optimization and design of geodetic networks*; Springer, 1985; pp. 363–428.
33. Grafarend, E.W. Three-dimensional deformation analysis: Global vector spherical harmonic and local finite element representation. *Tectonophysics* **1986**, *130*, 337–359.
34. Dermanis, A.; Grafarend, E. The finite element approach to the geodetic computation of two-and three-dimensional deformation parameters: A study of frame invariance and parameter estimability. International Conference "Cartography-Geodesy", Maracaibo, Venezuela, 1992.
35. Marot, C.; Pellerin, J.; Remacle, J.F. One machine, one minute, three billion tetrahedra. *International Journal for Numerical Methods in Engineering*, *0*, [https://onlinelibrary.wiley.com/doi/pdf/10.1002/nme.5987]. doi:10.1002/nme.5987.
36. Gere, J.M.; Goodno, B.J. Mechanics of Materials, Brief Edition. *Cengage Learning* **2012**.
37. Clemants, S.; Moore, G. Patterns of species diversity in eight northeastern United States cities. *Urban habitats* **2003**, *1*.
38. Raudsepp-Hearne, C.; Peterson, G.D.; Bennett, E.M. Ecosystem service bundles for analyzing tradeoffs in diverse landscapes. *Proceedings of the National Academy of Sciences* **2010**, *107*, 5242–5247.

39. Dossa, L.H.; Abdulkadir, A.; Amadou, H.; Sangare, S.; Schlecht, E. Exploring the diversity of urban and peri-urban agricultural systems in Sudano-Sahelian West Africa: An attempt towards a regional typology. *Landscape and urban planning* **2011**, *102*, 197–206.
40. Laliberté, E.; Legendre, P. A distance-based framework for measuring functional diversity from multiple traits. *Ecology* **2010**, *91*, 299–305.